UNIVERSITY OF WYOMING

SCHOOL OF ENERGY RESOURCES
CENTER FOR ECONOMIC GEOLOGY RESEARCH

WORKING PAPERS

NO. 1

Working Paper Title:

Interpreting wide-azimuth P-wave seismic data for reservoir properties related to faulting, fracture density and orientation – An example from the CO_2 storage site at Dry Fork Station near Gillette, Wyoming.

Yuri Ganshin and Charles Nye | 2021

CENTER FOR ECONOMIC GEOLOGY RESEARCH WORKING PAPERS

DIRECTOR: DR. J. FRED MCLAUGHLIN

About the University of Wyoming School of Energy Resources' (SER) Center for Economic Geology Research (CEGR) Working Paper Series

CEGR, which is one of SER's Centers of Excellence, investigates solutions to the challenges in Wyoming's fossil fuel and mineral industries. CEGR research projects explore opportunities to use Wyoming's distinctive geology and resources in order to develop those opportunities, diversify Wyoming's economy, and to maintain competitiveness in a low-carbon fossil energy future.

The objective of the CEGR Working Paper Series is to share "works in progress". The authors of the papers are solely responsible for the content of their contributions. The working papers can be found at https://www.uwyo.edu/cegr/research-projects/publications/

For more information about CEGR, please visit the CEGR web site at www.uwyo.edu/cegr.

UNIVERSITY OF WYOMING
School of Energy Resources
Center for Economic Geology Research

Interpreting wide-azimuth P-wave seismic data for reservoir properties related to faulting, fracture density and orientation – An example from the CO_2 storage site at Dry Fork Station near Gillette, Wyoming.

By Yuri Ganshin and Charles Nye

Abstract

The University of Wyoming School of Energy Resources' Center for Economic Geology Research is investigating a site for carbon storage near Basin Electric's Dry Fork Station (DFS), a lignite-fueled electric power station in Wyoming's Powder River Basin. The project seeks to mitigate carbon dioxide emissions from the use of fossil fuels by storing CO_2 deep underground in saline aquifers. Three subsurface reservoirs within the study area are being analyzed for their suitability for long-term carbon storage. The intensity and orientation of natural fractures within a reservoir and the associated seal determine flow-pathways for the injected CO_2 and thus govern the economic efficiency and long-term effectiveness of CO_2 storage.

The presence of natural fractures affects seismic wave propagation causing anisotropy that is related to the fracture orientation and intensity. The role of anisotropy in fracture detection has increased dramatically with the recent advents in wide-azimuth seismic acquisition and horizontal transverse isotropy (HTI) anisotropic theory describing seismic velocity variation with azimuth. We have developed a workflow to estimate fracture density and orientation based on high-density and high-resolution (HDHR) automated velocity analysis applied to azimuth-sectored common-mid-point (CMP) gathers. We implement this workflow with wide-azimuth, prestack DFS 3D reflection seismic data acquired during the fall of 2020. The azimuthal velocity analysis results agree with the orientation of lineaments interpreted from Landsat imagery, which confirms the effectiveness of our technology.

Discoveries from this work have improved the understanding of reflectors, faults, fracture zones, and other structural features at this carbon storage site. The poststack seismic amplitude volume was used to calculate 3D cubes of a reflector's surface curvature, dip and azimuth. We used these seismic attributes to delineate faults and fracture zones propagating along the target reservoir and seal horizons. Seismic attribute analysis presented in this paper, revealed several structural features in the DFS storage complex. These features show that potential subsurface

pathways for migration of CO_2 and displaced fluids may exist and should be further studied. A number of blind faults, including those of sub-seismic scale, were interpreted using horizon-based analysis. Two different fault-generation mechanisms were revealed in this study, namely basement-involved faulting and rock salt dissolution. The presence of these faults represents additional risk factors that have to be assessed by upcoming project activities at DFS, but which once completely addressed could result in a safer project.

Introduction

Understanding the behavior of CO_2 injected into a reservoir and delineating its spatial distribution are fundamentally important in carbon capture and sequestration (CCS) activities. Successful long-term sequestration of CO_2 relies upon understanding how geologic formation heterogeneity will affect fluid and pressure movements in the reservoir. This paper presents the results of utilizing the coherence and azimuthal velocity analyses of 3D reflection seismic data to identify faults and fracture zones near a new stratigraphic test well (UW PRB #1) drilled at DFS, north of Gillette, Wyoming.

Fluid injection in deep sedimentary formations with relatively low permeability might trigger slip on preexisting, unidentified faults (Zoback and Gorelick, 2012). As large-scale CO_2 injection in a saline aquifer proceeds, fluid pressure can increase in the subsurface and can potentially reactivate faults (Pawar et al., 2015). During the past decade, a number of induced seismic events have occurred in regions with historically low rates of seismicity, largely in the Midwest United States. In particular, Oklahoma experienced a rapid increase in the number and magnitude of earthquakes (Walsh and Zoback, 2015). These events have been attributed primarily to injection of brines into saline aquifers (Keranen et al., 2014), which increases the pore pressure and may cause critically stressed faults to slip. Some authors argue that sequestration of supercritical CO_2 in deep saline formations poses similar risk because of widespread pressure buildup associated with injection of large volumes of carbon dioxide at high rates (e.g., Zoback and Gorelick, 2012).

Faults reactivation poses some risk to storage sites through earthquakes but the primary motivation for finding blind faults, is the change in permeability which can threaten the seal integrity of the CO_2 repository (Zoback and Gorelick, 2012). Faults with large magnitude of displacement or those that have been mapped at the surface, can be easily identified during

geophysical site characterization studies and avoided. This study proposes a method for finding much smaller faults, especially those that do not have exposure at the surface (i.e., blind faults) or those with small displacement magnitude that can't be identified on typical seismic-amplitude sections (sub-seismic faults).

Faults caused by large-scale deformations in the earth are traditionally identified from stacked seismic sections by visual interpretation, while small displacement faults (of sub-seismic resolution) can be smoothed out during data processing and are generally difficult to observe directly on a seismic section. Small-displacement faults cause very slight offsets in reflectors that appears on seismic data as "an inconsequential disruption" (Chopra et al., 2000). Nevertheless, deformations of sub-seismic scale can account for up to 50% of the total subsurface strain and have strong effects on reservoir compartmentalization and fluid flow (Endres et al., 2005; Marret and Allmendinger, 1991; Walsh et al., 1998). With the invention of horizon-based and volumetric seismic attribute analyses techniques (Chopra et al., 2001; Roberts, 2001), there is a continuously increasing number of researchers who have successfully tackled the problem of finding sub-seismic faults and fracture networks in unconventional reservoirs (Blumentriff et al., 2007; Chopra et al., 2000; Chopra and Marfurt, 2007; Endres et. al., 2005; Kazmi et al., 2012; Mai et al., 2009; Aarre et al., 2012; Michelena et al., 2013; Calvert et al., 2008; Jenner et al., 2001).

Sub-seismic faults with associated fractured damage zones (Johri et al., 2014) can be identified through the horizon-based analyses of coherence/curvature volumes derived from post-stack reflection seismic data (Chopra et al., 2011). Attribute calculations, such as coherence and curvature, identify subtle changes in the dataset that conventional interpretation of seismic cross-sections might overlook. Coherence, dip, and azimuth maps can highlight subtle faults having throws of less than 10 msec as well as stratigraphic features that manifest themselves through differential compaction or subtle changes in the seismic waveform (Marfurt, 2006).

Seismic anisotropy analysis looks at directionally dependent variations in the wave propagation velocity (the velocity variation with azimuth, VVAZ technique). Fractures slow the propagation velocity of wave if the fractures are perpendicular to the wave direction (Williams and Jenner, 2002). When the wave propagation path is parallel to the fracture direction, the velocity remains unaffected. This is the basic principle of fracture detection with a wide-azimuth

(WAZ) seismic data. Vertical or near-vertical fractures cause seismic travel time to vary with source-receiver azimuth.

A combination of attribute calculations and anisotropy data can detect locations of faults within a region, estimate fracture intensity, and determine fault/fracture orientation. Knowing the location of fractures and their orientations allows for the assessment of reservoir quality, aids in planning of injection well placement, and may serve as a predictor of injection/production rates.

Geologic Setting

The structural extent of the central portion of the Powder River Basin (PRB) is bounded by two Laramide-age uplifts: the Bighorn Mountains on the west and the Black Hills on the east. The PRB is an asymmetric syncline, with steeply dipping strata along the western limb and gentle dips in the central and eastern parts of the basin (Figure 1). The basin axis trends northwest-southeast along the Bighorn Mountains.

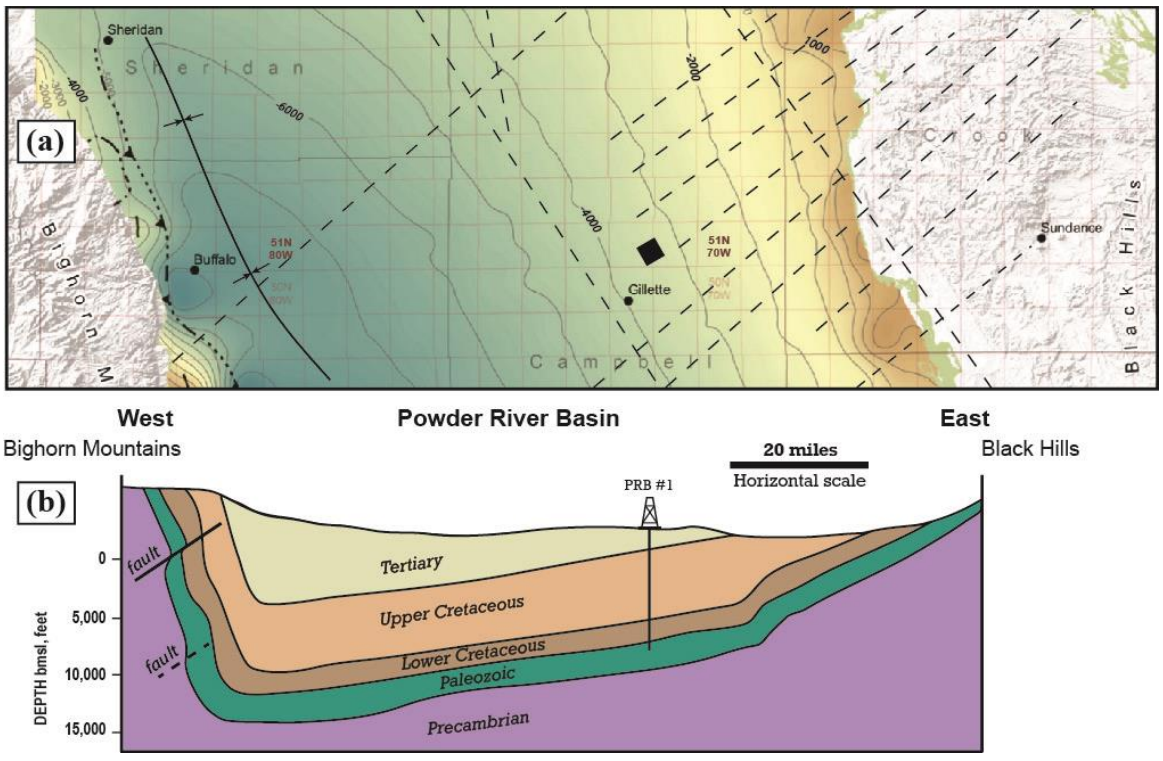

Figure 1. (a) Structure map of the Muddy Sandstone with the contours drawn every 1,000 feet (modified from Lichtner et al., 2020). Lineaments (dashed lines) are from Anna (2009). The black square north of Gillette indicates the location of the DFS-3D seismic survey. (b) Generalized east-west cross section of the central Powder River Basin (modified from Anna, 2009) with approximate location of the UW PRB #1 stratigraphic well.

Similar to many other Rocky Mountain foreland structural basins, the PRB developed during the Laramide orogeny. The basin's deepest part can exceed 17,000 ft to the top of the Precambrian basement (Anna, 2009). These basement rocks are located 12,000-12,500 ft below the land surface in the PRB #1 well's vicinity on the eastern limb of the syncline. In the study area, the regional dip is about 100 ft/mi (~1˚) to the west (Figure 1-b).

Past work in the PRB, has identified numerous linear surface features which indicate the presence of faults, fold belts, shear zones, or other zones of weakness in the Precambrian basement rocks which were activated during the Laramide orogeny (Marrs and Raines, 1984; Anna, 2009). In the central PRB, most structures are oriented northwest-southeast and northeast-southwest, a trend which is commonly associated with major tectonic elements throughout the Rocky Mountain area (Figure 1a). For example, Thomas (1971) summarized the tectonics of southwest Wyoming as a set of northeast- and northwest-trending plates bounded by lineaments that respond to compressional forces by combined action of pure shear and plate coupling. Based on analysis of Landsat images, Marrs and Raines (1984) have found the trends of the linear features to fall generally within two populations, one trending N12˚-53˚W, the other trending N30˚-85˚E. It was shown that the lineaments defined through the analysis of Landsat images correlate with bedrock and surficial geology maps, gravity and magnetic data, isopach maps, and maps of petroleum production (Marrs and Raines, 1984). As shown by Anna (2009), the Upper Minnelusa oil fields are generally aligned with this prevailing trend, thereby demonstrating the structural control on the orientation of reservoir rock deposition. Also, the same structural trends are assumed to be associated with zones of structural deformation and could be areas of enhanced secondary porosity and permeability in the Cretaceous-age formations. For example, zones with high concentrations of lineaments in the central PRB correlate with Mowry Shale sweet spots where increased fracture intensity enhances oil and gas production (Anna, 2009). These findings lead to the conclusion that lineaments in the study area may be used as guides in determining hydraulic connectivity (or establish its absence) at the proposed CO_2 sequestration site.

The Wyoming CarbonSAFE project team has evaluated the geology of the DFS storage complex including several storage reservoirs and over 4,000 feet of associated caprock (McLaughlin, 2021). First-stage pre-feasibility geologic evaluations were focused on assessing

four potential storage reservoirs within the complex – the Minnelusa Formation, the Lower Sundance Formation (Hulett and Canyon Springs Members), the Lakota/Fall River Group, and the Muddy Sandstone. Site specific data, particularly core and log data collected from UW PRB #1, allowed the project team to focus on the storage site's highest priority injection zones, the Minnelusa Formation and the Hulett Member of the Lower Sundance Formation (Figure 2).

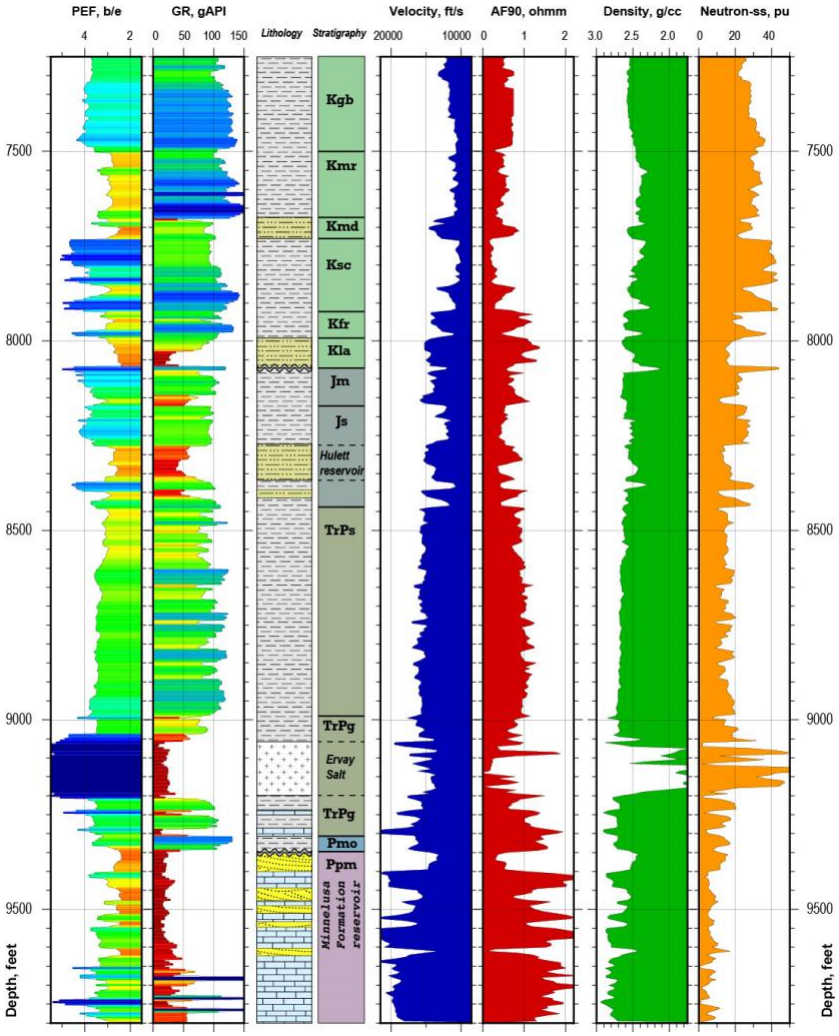

Figure 2. Interpreted wireline logs from UW PRB #1 (API 572720). The currently favored injection zones are the Minnelusa Formation (Ppm) and the Hulett Member of the Lower Sundance Formation (Js). The confining layers shown in this figure include the Cretaceous Belle Fourche (Kgb), Mowry (Kmr), and Skull Creek (Ksc) shales, siltstones and mudstones within Morrison (Jm) and Upper Sundance formations, Triassic Spearfish (TrPs) and Goose Egg (TrPg) formations, and the Opeche Shale (Pmo) which includes shale, carbonate, siltstone, mudstone and evaporate units that overlie the Minnelusa Formation.

Characterization of associated caprock/confining layers included analysis of capillary properties, mineralogy, pore throat-radius distribution, log- and lab-measured porosity/permeability, fluid

inclusion volatiles, and rock strength measurements. The local and regional continuity of the confining layers was evaluated using log and 2D reflection seismic data. These data were used to characterize micro- and meso-scale heterogeneities, porosity, permeability, sealing capacities, and sealing performance through geologic time. All the above-mentioned analyses suggest that each seal identified at the DFS storage complex provides an effective fluid barrier, capable of long-term retention of injected fluids. These data show no physical evidence of vertical fluid migration between target reservoirs or upward into seals, suggesting that the seals have acted as fluid barriers throughout geologic history. This historical integrity indicates that if there were no structural features at the site then CO_2 could be safely stored at this site at any sub-fracturing injection pressure. An interpretation of newly acquired three-dimensional reflection seismic data from the DFS site was undertaken to determine what structural faults and fractures might change this otherwise excellent reservoir integrity, and to avoid those faults and fractures when choosing the best locations for CO_2 injection wells.

WAZ data conditioning and analyses

During the fall of 2020, 3D reflection wide-azimuth (WAZ) seismic data were acquired by the Dawson Geophysical company around the Basin Electric's Dry Fork Station. The objective was to characterize potential reservoirs in tight sands where natural fractures could significantly affect the CO_2 storage assessment. Survey acquisition parameters included the use of four AHV IV Commander vibrators, GSR recording system, a ~11,500 ft maximum source-receiver offset, a ~300x nominal common mid-point (CMP) fold coverage, and 110 x 110 feet CMP bin size. More details on the data acquisition parameters can be found in Table 1. The stacked amplitude volume was prepared using an amplitude preservation process and migrated using Kirchhoff pre-stack time migration (PSTM). The seismic volume comprises 145 inlines and 148 crosslines, of which only 111 central inlines and 111 crosslines were selected for interpretation (to avoid low-fold areas). The seismic datum is 4500 feet. The grid definition (seismic inline and crossline binning scheme) and common-mid-point (CMP) coverage map is shown in Figure 3. The five-dimensional interpolation technique was used to tackle the problem of infilling acquisition gaps and irregular surface observations. This technique assumes simultaneous data interpolation in all five seismic dimensions (time, inline, crossline, offset, and

azimuth) and has great utility in predicting missing data with correct amplitude and phase variations.

Design parameter	Value
Total surface coverage	9.0 sq miles
Receiver interval	220 feet
Receiver line interval	660 feet
Receivers per square mile	203.3
Total receivers	1,850
Source station interval	220 feet
Source line interval	660 feet
Sources per square mile	197.8
Total source points	1,800
Seismic record length	6 sec
Sample interval	1 ms
Recording geometry	Static
Roll on & roll off	No
Bin size	110 x 110 feet
Geophones per point	6
Sweep length	12 sec
Number of sweeps	2
Vibrators / Array	4
Fold – all offsets	298-306

Table 1. Seismic acquisition parameters for the DFS 3D survey.

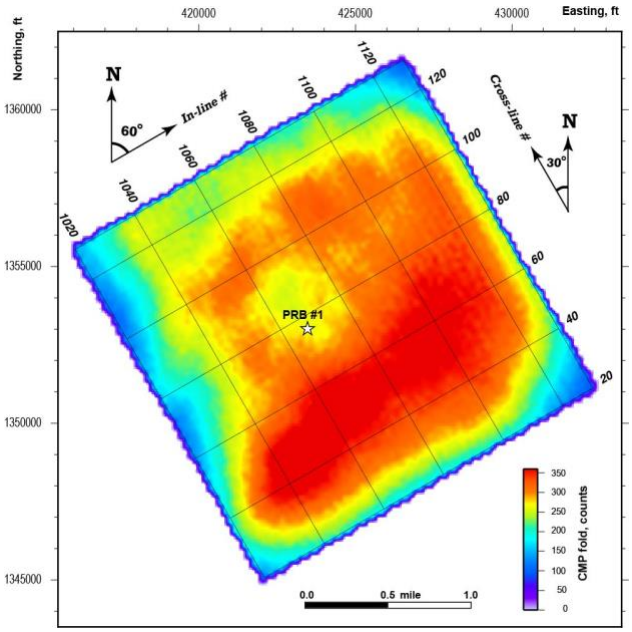

Figure 3. CMP coverage over the survey area selected for interpretation (~2.3 x 2.3 miles).

Importantly, the 5D interpolation can successfully interpolate sparse data, improve velocity analysis, and reduce acquisition and migration artifacts. Based on the results presented below the 5D interpolation procedure, utilized by the Dawson processing team, appears to have dramatically improved the continuity of seismic reflections and the overall signal-to-noise ratio. Besides 5D interpolation, the prestack data conditioning for velocity analysis consisted of refraction statics, denoising, surface-consistent amplitude correction and deconvolution, and Kirchhoff prestack time migration output to CMP gathers. CMP gathers conditioned with the above-described workflow show well-defined P-wave reflections and semblance maxima in the velocity spectral display, as illustrated in Figure 4.

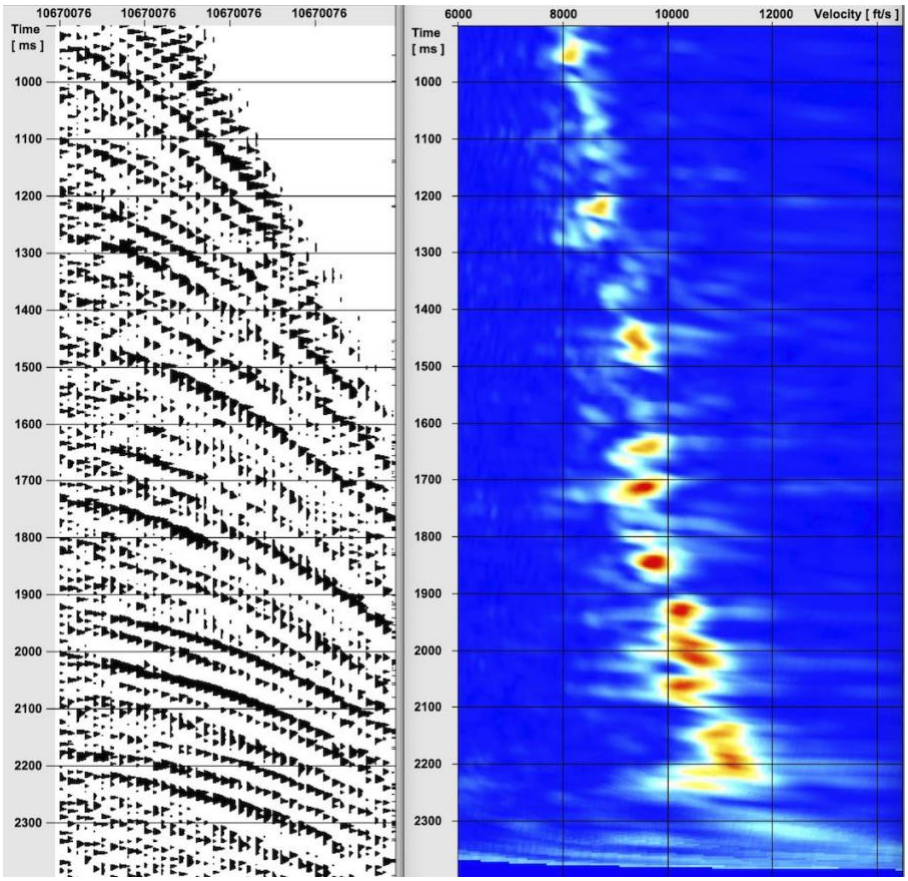

Figure 4. Velocity spectra derived from the CMP gather corresponding to the PRB #1 well location in Figure 3.

Velocity analysis is one of the most important steps in seismic processing. There are two kinds of velocity analysis, one for producing the best stacked image in time domain (stacking velocity), and another for getting a depth velocity through depth migration. In this paper we will

consider only stacking velocities. The approximated kinematic behaviors of the moveout correction for P-wave reflection traveltime are defined by either hyperbolic (Dix, 1955) or nonhyperbolic equations (Alkhalifah and Tsvankin, 1995; Alkhalifah, 1997). The Dix's formula has been derived for infinitely small source-receiver separation and for a 1-D velocity model, that is for the model with horizontal homogeneous layers. This formula is restricted to small offset-to-depth ratio and produces erroneous results with increasing offset and/or anisotropy (increased number of beds). The most common nonhyperbolic equations use three parameters: (1) the two-way traveltime at zero offset, t_0, (2) the short-spread normal-moveout velocity, V_{nmo}, and an effective anisotropy parameter η. For the purpose of this study, we used the nonhyperbolic moveout equation proposed by Fomel (2004) to obtain dense model parameters by simultaneously picking velocity and anisotropy parameters. The objective is to find parameters that produce maximum stacking power at a specific t_0. To handle the vast amounts of pre-stack seismic data (CMP gathers) we used an automated velocity analysis application which had been previously developed at the University of Wyoming (https://www.uwyo.edu/cegr/software/). Not only did this automation simplify the onerous task of manual picking, but it also allowed velocity analysis to be performed for every CMP bin with no abstraction. That led to what is frequently termed in geophysical publications as "high density high resolution" (HDHR) velocity analysis in which analysis is carried out at every spatial bin (or CMP) and every time sample down the record. For processing purposes, a denser lateral and temporal sampling is invariably useful in further enhancing the statistical base of the dataset, thus, in reducing the resultant velocity uncertainty.

To analyze Velocity Variations with Azimuth (VVAz) using the high-fold WAZ data we followed the conventional approach to separate the seismic data into a number of azimuth sectors and process each sector independently by picking semblance maxima at various azimuths. We choose to split seismic data into six sectors and to perform HDHR automated velocity analysis applied to the azimuth-sectored common-mid-point (CMP) gathers. Six partially overlapping azimuth sectors centered at 15˚, 45˚, 75˚, 105˚, 135˚, and 165˚ were generated (Figure 5) and the automated velocity analyses were performed independently for each of the sectored datasets. We used enlarged datasets (60˚ each) with overlapping sectors to achieve an evenly populated distribution of offsets for all azimuthal sectors (Figure 6).

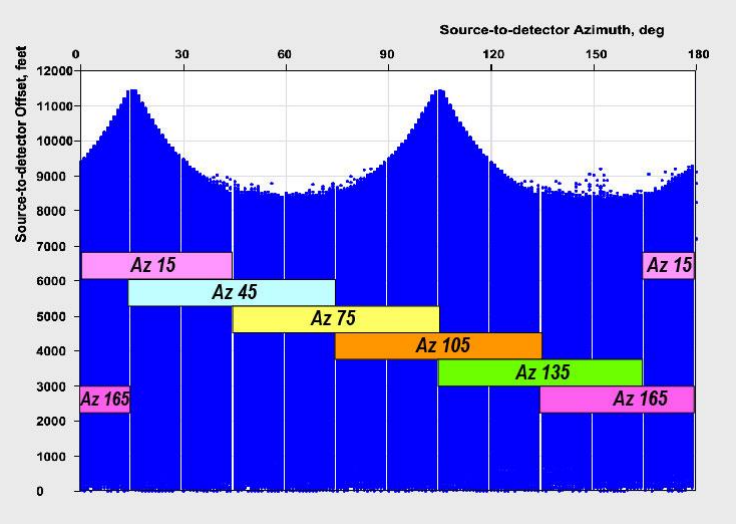

Figure 5. Source-to-receiver offset vs. azimuth scatter diagram for the DFS-3D seismic survey and azimuthal selection scheme. Note that all figures use the seismic survey azimuth convention where 90 degrees corresponds to north, and 180 degrees corresponds to west.

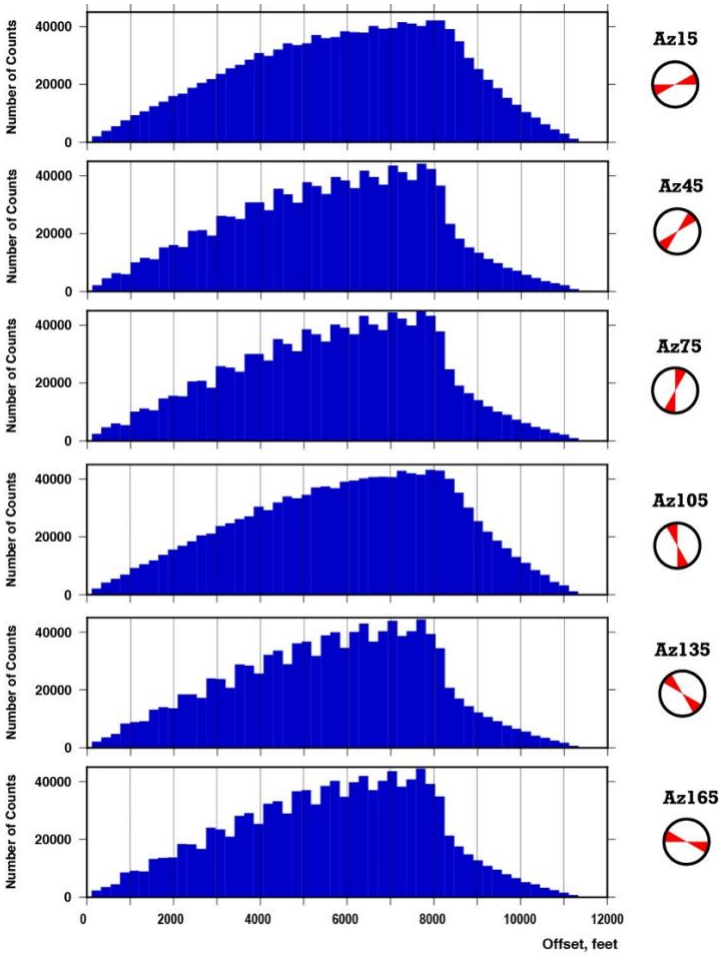

Figure 6. Frequency of source-to-receiver offset occurrence for the six azimuthal selections.

The azimuthal variation in normal-moveout velocity can be described by an ellipse in the horizontal plane. For a single set of vertical fractures, the fast velocity will be equal to the bulk rock velocity and will be oriented parallel to the fractures. Grechka and Tsvankin (1998) showed that an ellipse in the horizontal plane describes the azimuthal variation of V_{nmo} even if the medium is arbitrarily anisotropic and heterogeneous. Therefore, we fitted an elliptical curve to the six velocity values selected from the corresponding samples of azimuthal velocity volumes, to give the fast, V_{fast}, and slow, V_{slow}, velocity values and the corresponding azimuths. The fracture intensity (anisotropy percentage e) can then be obtained by dividing the difference between the fast and slow velocities by the isotropic (fast) one (Dulaijan and Margrave, 2015)

$$e = \frac{100\times(V_{fast}-V_{slow})}{V_{fast}} \quad (1)$$

To get reliable estimates of fracture properties, the anisotropic parameters must be characterized with dense enough analysis to capture the variability of the earth's anisotropy. The HDHR velocity analyses performed for this study at every data sample of the sectored datasets, allowed minor data smoothing with an operator that was small enough to provide legible, high resolution fracture analysis with low uncertainty.

Our specific objective in this study was to apply selected seismic attributes to aid in quantifying the reservoir properties and lateral continuity of CO_2 sequestration targets. We computed multiple morphological and physical seismic attributes for the whole seismic volume: among possible attributes we analyzed were: instantaneous and RMS amplitude, instantaneous and mean frequency, coherency and curvature, dip azimuth and dip magnitude, velocity, and acoustic impedance. Among the morphological attributes, curvature, dip azimuth, and dip magnitude were particularly useful in mapping structural trends and imaging liner features within the target horizons.

Curvature Attribute. In a general sense the seismic curvature attribute is a measure of how deformed a reflecting surface is at a particular location. The more deformed the surface, the larger its curvature. With respect to geometry, curvature is defined as the reciprocal of the radius of curvature, and correspondingly, belongs to the geometrical category of attributes. The suite of curvature attributes utilized in this study, comprises dip magnitude, dip azimuth, maximum and minimum, and strike and dip curvatures. Analysis of these attributes can help remove the effects of regional dip and emphasizes small-scale features such as tight folds, faults, karst zones, and fractures.

The estimation of volumetric curvature attributes is performed in three stages. First, for each volume sample, a small reflection surface (3×3 horizontal samples) is identified around the central sample. The surface Z-positions are calculated by finding the maximum cross-correlation value over a vertical analysis window between the central trace and each surrounding trace. A parabolic fitting technique is used for precise time shift (tilt) identification that corresponds to the maximum value of the cross-correlation between the discrete trace samples. Next, a least-squares quadratic surface Z (X, Y) is fitted to the data within the analysis range. Finally, the set of curvature attributes is computed from the coefficients of the quadratic surface using traditional differential geometry (Roberts, 2001). At any point of the surface, the curvature (positive or negative) can be measured at any azimuth. One of these azimuths will yield the largest curvature. This curvature is named the *maximum curvature* and the curvature at the orthogonal azimuth is named the *minimum curvature*. The *maximum* and *minimum curvature* attributes are very effective at delimiting faults and fault geometries, with maximum curvature corresponding to the up-thrown (positive) side of a fault. The curvature attribute extracted in the direction of maximum dip is named the *dip curvature*, while the one extracted in the orthogonal direction (along strike) gives us the *strike curvature*. The last two attributes can be especially useful in examining the local surface morphology and interconnectivity that can help explain buoyancy-driven processes and fluid migration pathways. The curvature attributes described above are lateral second-order derivatives of structural relief components of the seismic reflection events. Being a second derivative results in great sensitivity to subtle structural variations. In contrast, the *dip magnitude* and *dip azimuth* are derived using first-order derivatives, which allows their use for determining regional structural trends.

The curvature attributes can be related to the fracture intensity assuming that brittle rock fractures in response to applied stress, which in turn, correlates with fracture intensity (Nelson, 2001). In this study, we use curvature attributes as tools for fracture-zone detection with the additional assumptions that fracture zones are seismically detectable with widths comparable in size with the Fresnel zone diameter.

One of the most effective methods for visualizing the curvature attribute is to use time or horizon slicing because faults and fractures typically cross multiple strata, particularly for steep-dipping and strike-slip faults. Sequential slicing through curvature volumes can interactively reveal structural features in a map view. The maps are either a time slice or a horizon slice at a

stratigraphic level of interest. To avoid confusing curvature with regular seismic amplitude or other discontinuity measures, we intentionally show curvature in red-and-blue colors. This visualization convention defines two complimentary components of fractured reservoirs. The anticlinal crests of a reservoir is associated with the high curvature (blue), whereas synclinal features have negative curvature (red). The faults are usually located at the edge or at the boundary between the positive and negative curvature. In other words, curvature is not really highlighting major discontinuities but rather the coherent portion of folds on either side. This allows detection of faults and fractures even where no major faults are visible from regular seismic amplitudes.

Fault and Fracture Interpretation

Discontinuity analysis.

The prospective injection zones and the major confining layers are picked and indicated on the stacked sections in Figure 7. The upper member of the Minnelusa is divided into five sabkha cycles: A, B, C, D, and E, with E being the oldest one. Each depositional cycle consists of a basal dolomite and overlying sandstone (Figure 2). At UW PRB #1 the A sabkha cycle has been interpreted to be unconformably absent (McLaughlin, 2021). Sandstone reservoirs of the upper member of the Minnelusa Formation are sealed by Opeche shales of the Goose Egg Formation. Another member of the Goose Egg Formation, the Ervay Salt, can be recognized in borehole geophysical logs, and especially on the density log (Figure 2). Subsurface water invasion can readily dissolve the Ervay Salt to produce cavities which subsequently collapse. These collapse can produce salt-dissolution faults with significant geomorphic expression. Much shallower in the rock section, the Hulett sandstone member of Sundance Formation includes marine sandy beds consisting mainly of fine- and very fine grained, moderately sorted, calcareous sandstone. Overlying the Hulett is transgressive gray to black Skull Creek Shale. The Skull Creek Shale consists of siltstone and mudstone which is the seal for the Hulett reservoir. The third possible CO_2 storage reservoir is formed by the Lakota and the Fall River Formation. Above the Lakota and Fall River reservoirs are both the Mowry and Niobrara Shales. The Mowry and Niobrara Shales represent extensive and seismically continuous regional seals. The package of shales which includes the Niobrara is many thousand feet thick and offers final protection of the shallower drinking water reservoirs if CO_2 were to migrate out of the deeper target reservoirs.

The fracture analysis performed in this paper considers the interval from the Niobrara Shale marker to the Cambrian marker. We use the abstract term "marker" to identify the approximate middle of a formation because several geologic features having thicknesses under a quarter of a wavelength were not resolvable. In this study, we have chosen the Cambrian marker to delineate basement-involved faults and fracture zones because the Cambrian is the last continuous reflection above the seismically transparent basement (Figure 7).

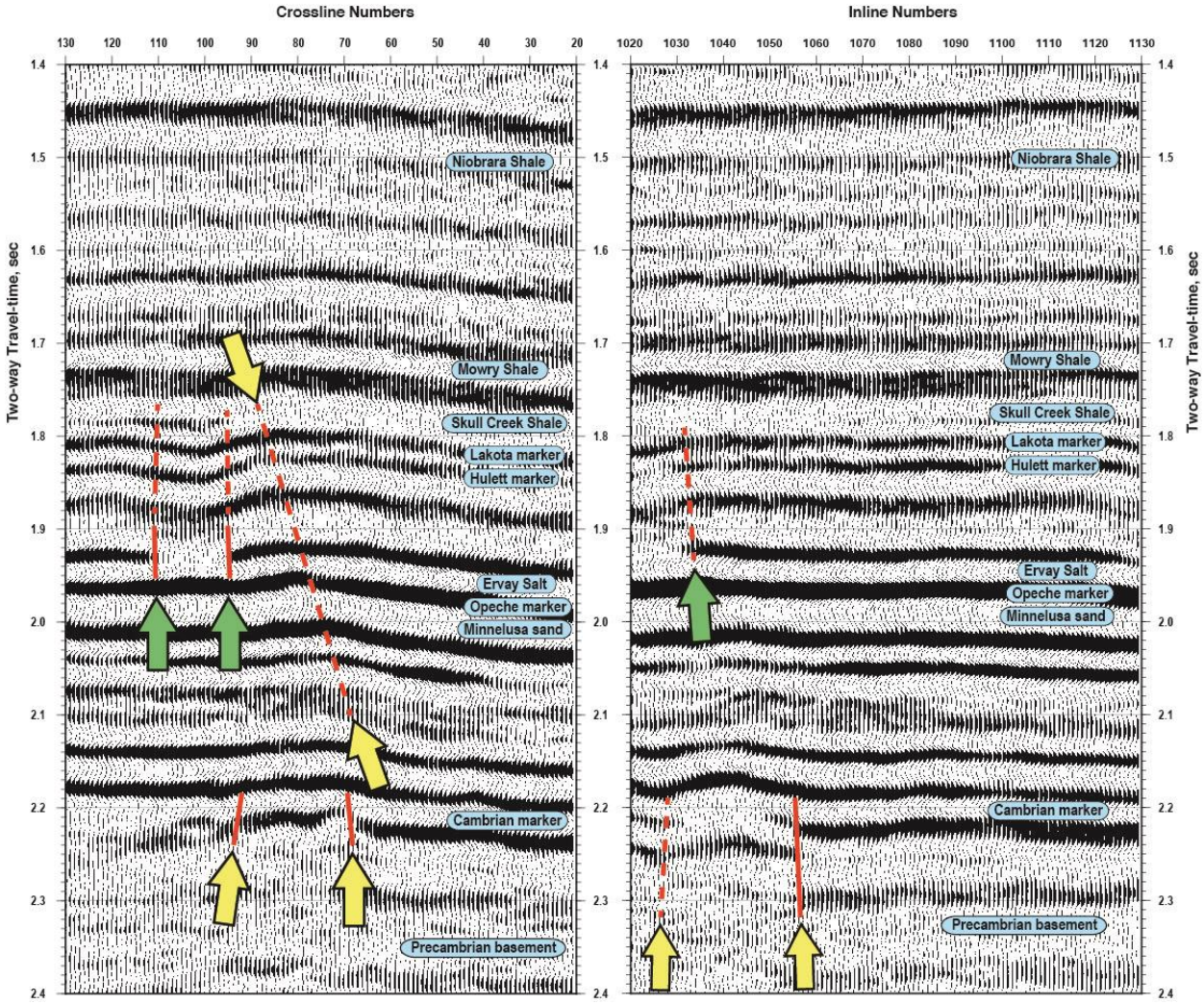

Figure 7. Interpreted stacked CMP sections: inline 1060 (left) and crossline 60 (right). See Figure 3 for the line locations within the DFS 3D survey. Two sets of structural features are indicated with the arrowheads: basement-involved faults and zones of fault reactivation (yellow color) and salt-dissolution faults (green color).

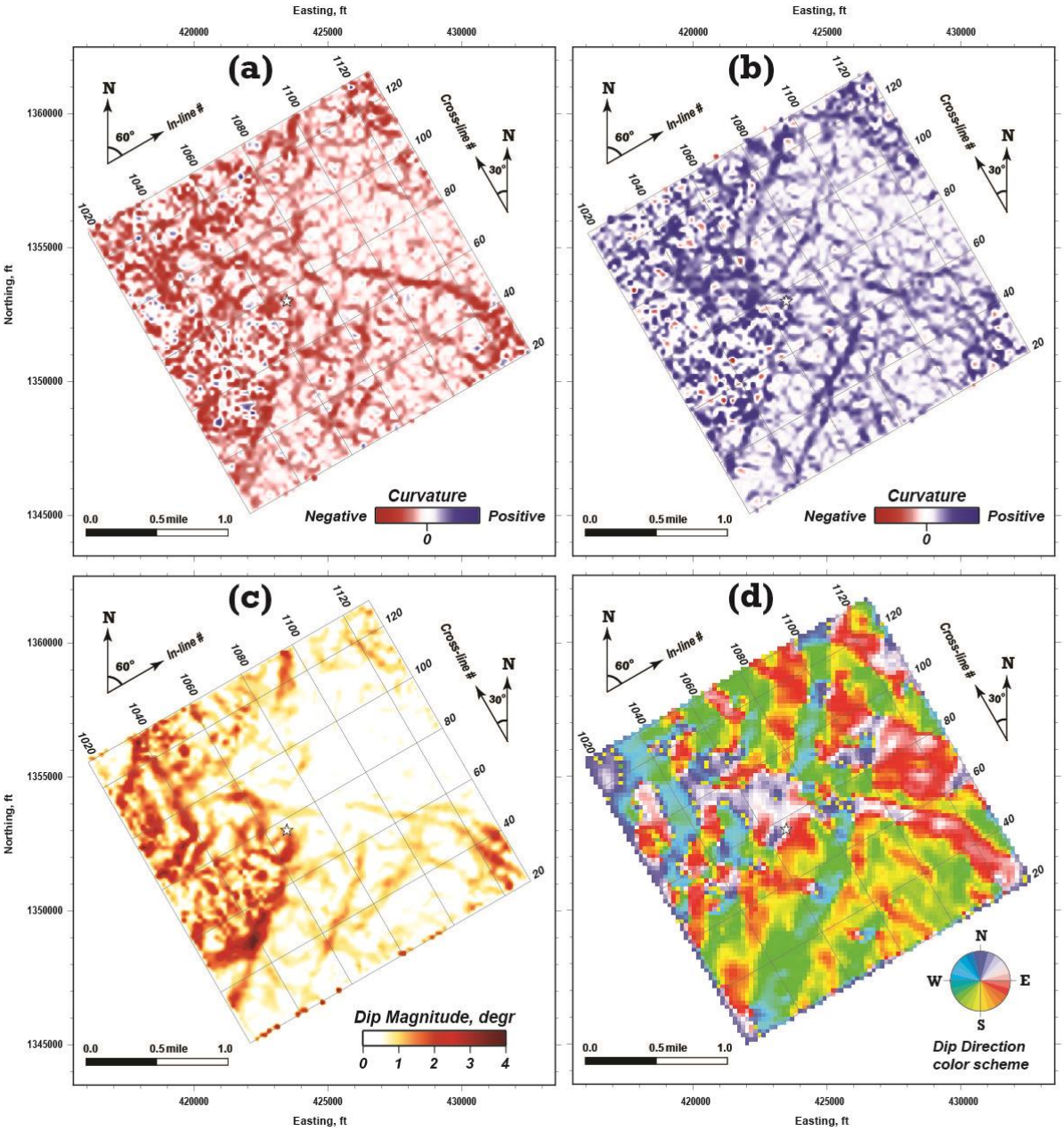

Figure 8. Horizon slices through volumetric calculations of (a) minimum, (b) maximum, (c) dip magnitude, and (d) dip azimuth curvature attributes along the Cambrian marker. Note the NE and NW trending linear features that can be observed in the slices. Coordinate projection: NAD-27, Wyoming East. The star symbol indicates PRB #1 well projection.

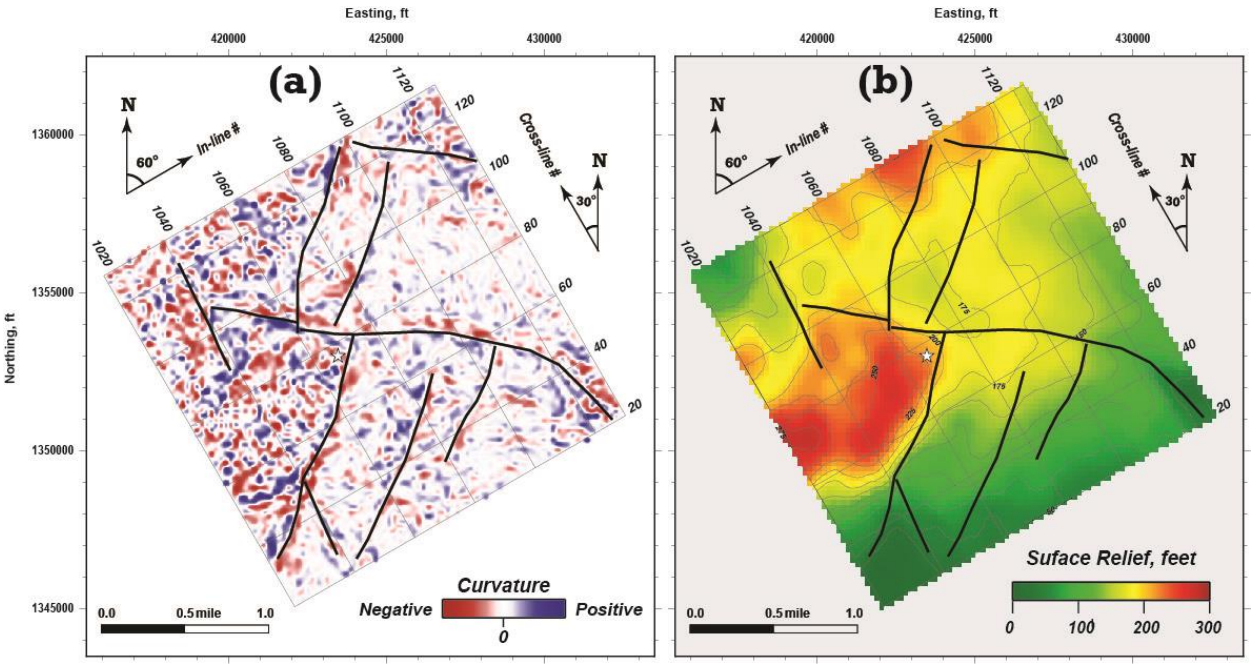

Figure 9. Horizon slice through volumetric calculation of dip curvature attribute (a), and structural relief map of the Cambrian marker. Black lines indicate fault traces interpreted along the Cambrian marker. The Cambrian surface structure map was calculated from the corresponding time structure map assuming average velocity of 15,500 ft/s, with the contours drawn every 25 feet. The star symbol indicates PRB #1 well projection.

Discontinuities in seismic reflectivity character are most readily apparent when presented along seismic horizons of interest in the form of attribute horizon slices. Figures 8 and 9a show horizon slices along the Cambrian marker through multiple curvature volumes that were prepared in the current study. These were maximum and minimum curvature, strike and dip curvature, dip magnitude, and dip azimuth volumetric attributes.

Although not shown for all target horizons, we also used slices through the coherence volume to validate the interpreted fault/fracture traces. Interpretation was performed manually using all available horizon slices, and the interpreted reflection discontinuities were updated iteratively. The resultant structural discontinuity lineaments for the Cambrian marker are shown with black lines in Figure 9. Figure 9b shows the interpreted linear features overlain on top of the Cambrian structural relief map where colors indicate difference in elevation relative to the lowest point on the surface (green color). We interpret these lineaments to be associated with the basement-block boundaries (basement-involved faults) that were replicated as a blocky depositional pattern for Cambrian sediments. One of the uplifted blocks is located just west of

the PRB #1 projection point and is characterized by two well-defined faults, one trending northeast and the other northwest (Figure 9b).

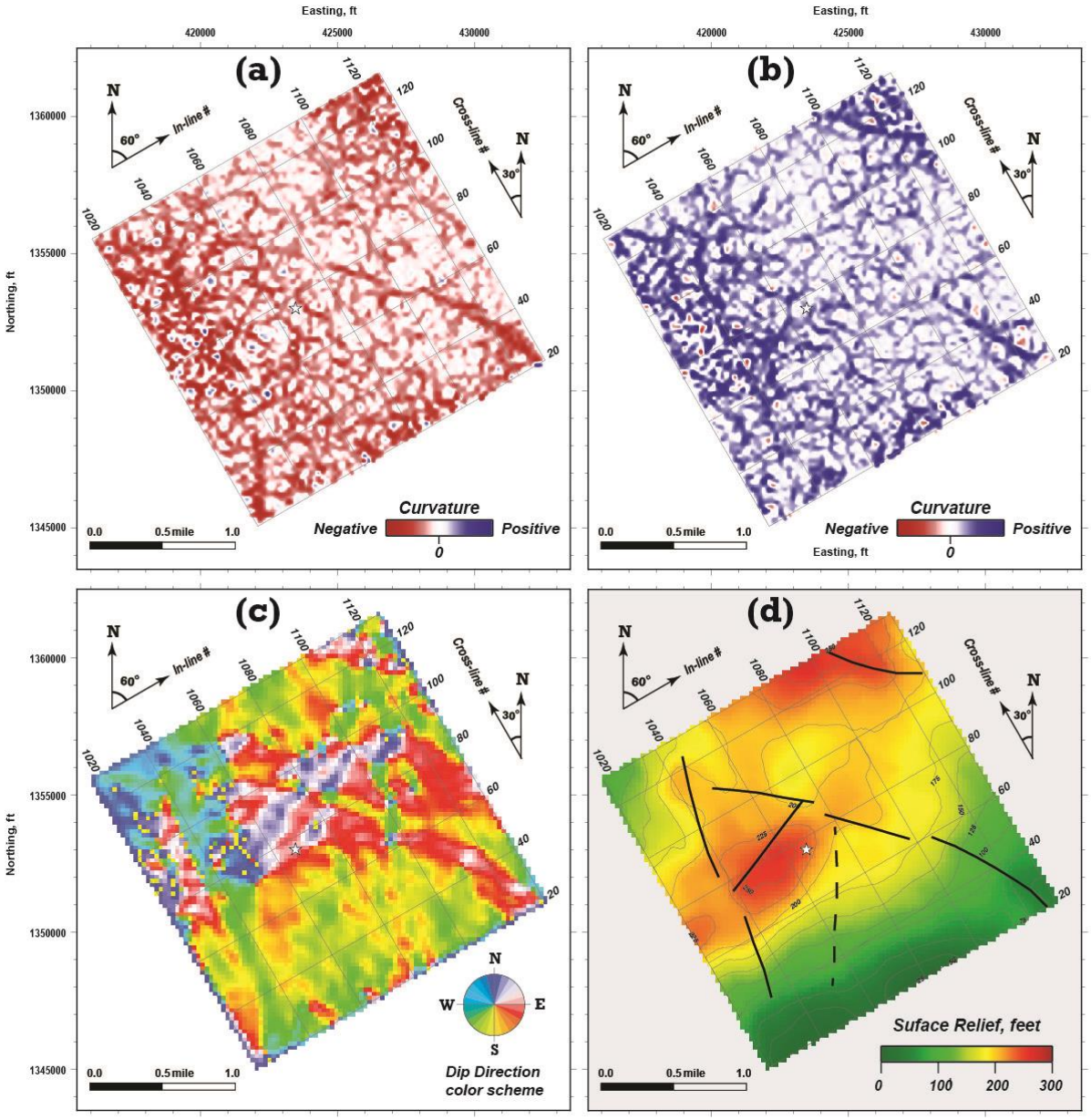

Figure 10. Horizon slices through volumetric calculations of (a) minimum, (b) maximum, (c) dip azimuth curvature attributes, and (d) structural relief map along the Minnelusa marker with interpreted fault traces (black curves). The surface structure map was calculated assuming average formation velocity of 14,500 ft/s, with the contours drawn every 25 feet. The star symbol indicates the PRB #1 well projection.

A similar structural analysis was performed along the Minnelusa marker. This marker approximates the center of the sandstone reservoirs of the upper member of the Minnelusa Formation. The horizon slices through volumetric curvature attributes together with the interpreted structural features for the Minnelusa are shown in Figure 10. There are a number of fault/fracture lineaments, some of which we tracked through the slices and displayed in black in Figure 10d. Note the northwest-trending lineament in the middle part of study area that correlates with a similar feature observed along the Cambrian marker. A dome-like structure west from the PRB #1 well also closely resembles uplifted block in Figure 9b.

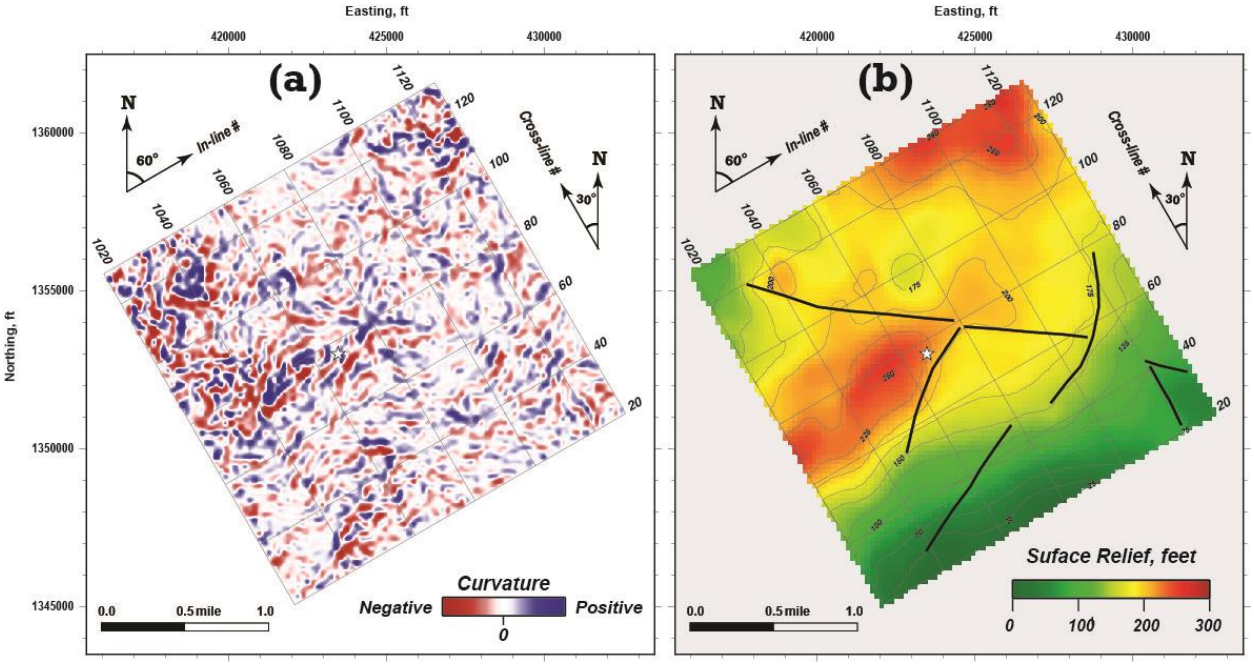

Figure 11. Horizon slice through volumetric calculation of dip curvature attribute (a), and (b) structural relief map of the Opeche marker. Black lines indicate fault traces interpreted along the marker. The surface structure map was calculated assuming average velocity of 14,500 ft/s, with the contours drawn every 25 feet. The star symbol indicates PRB #1 well projection.

Trapping mechanisms for the A and B sandstone reservoirs of the upper member of the Minnelusa Formation are mostly controlled by the Opeche Shale, an effective vertical and lateral seal. However, this shale formation is only about 34-feet thick in the study area, and we used the Opeche marker term to indicate a thicker stratigraphic interval within the Goose Egg Formation below the base of Ervay Salt Member (Figure 2). Dip curvature attribute extracted along the Opeche marker and the corresponding structural relief map with interpreted lineaments are

shown in Figure 11. Again, as for Minnelusa horizon, we can observe the large-scale northwest trending lineament just north from PRB #1 well. The dome-like uplift west from the well projection still remains a dominant structural feature that probably repeats tectonic architecture of Precambrian basement. Overall, large-scale basement-involved faults seem to characterize deformation structures associated with the Paleozoic sediments at the study site. The northwest trending fault just north of PRB #1 well is a large-scale structure that should be avoided if Minnelusa sandstones are chosen for CO_2 repository. However, a correlation between medium- and small-scale faults, cross-cutting the Paleozoic strata, is difficult because of their strong variation in orientation.

Figure 12 shows horizon slices along the Ervay Salt marker through the minimum and maximum curvature, and coherence volumes. No well-defined linear features can be observed in these attribute slices. Instead, there are several circular features ranging in size from about 200 to over 2,000 feet. We interpret these circular features to be subsidence features caused by exposure of this evaporitic formation to groundwater. The overlying formations droop into each dissolved feature in circural depressions, which produce stark changes in curvature and coherence attributes. This vertically propagating cavity or collapse chimney can be observed in vertical sections (Figure 7, green arrows). The high solubility and ductility of rock salts like the Ervay Salt supports this interpretation of dissolution subsidence features. The plastic behavior of rock salt is demonstrated worldwide by salt glaciers and by flowage patterns observed in salt domes. The ductile style of rock salt deformation also explains the absence of any interpretable linear faults in the Ervay Salt. However, the Ervay salt has been influenced by those basement-involved features, and retains the dome-like structural uplift west of the PRB #1 well (Figure 12d).

Discontinuity attributes extracted for the Hulett marker demonstrate a somewhat different set of structural features compared to previously discussed (Figure 13). There is no evidence of a large-scale, northwest-trending lineament north of PRB #1 well. Instead, we can observe several rounded features similar to those found along the Ervay Salt marker. We interpret these circular features as the salt dissolution faults that propagated vertically upwards from the Ervay Salt horizon. The depressed area inside the circles characterizes these sinkholes in the surface structure map (Figure 13-d). The area west of the PRB #1 well is comparatively elevated, showing that some large-scale features like basement-involved block persist in the Ervay Salt.

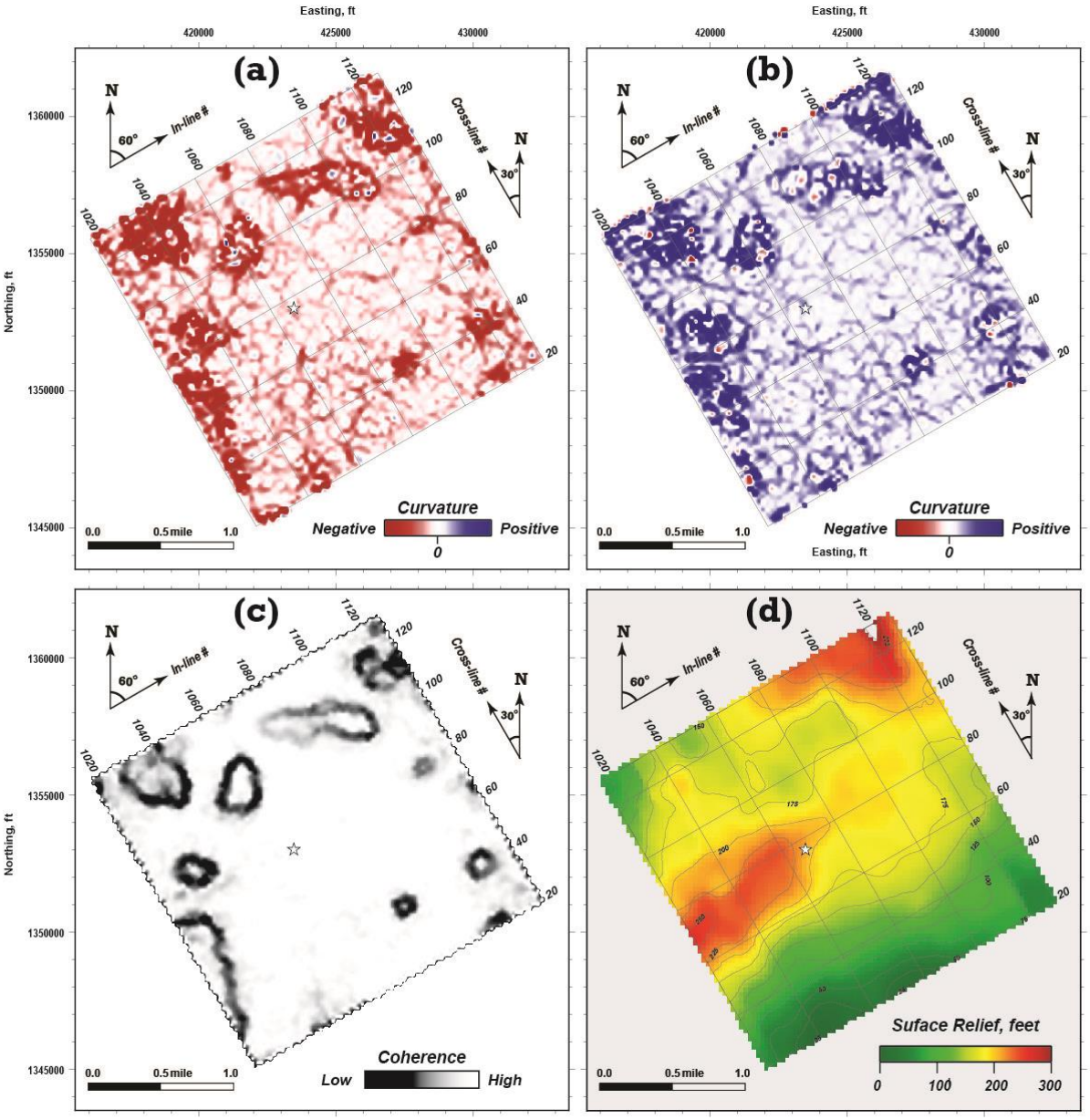

Figure 12. Horizon slices through volumetric calculations of (a) minimum and (b) maximum curvature attributes. (c) Coherence attribute slice, and (d) structural relief map along the Ervay Salt marker. The surface structure map was calculated assuming average formation velocity of 14,500 ft/s, with the contours drawn every 25 feet. The star symbol indicates the PRB #1 well projection

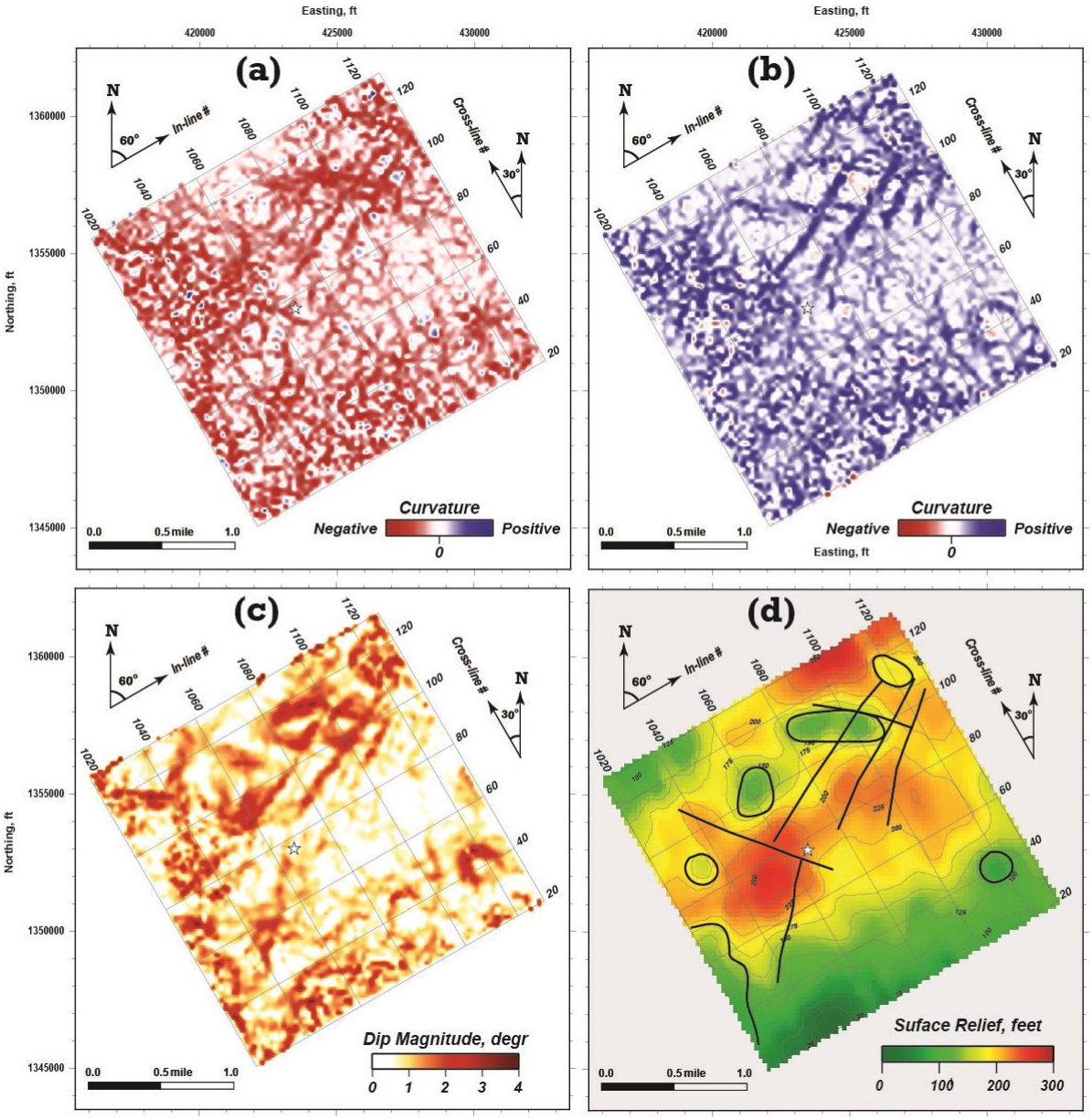

Figure 13. Horizon slices through volumetric calculations of (a) minimum and (b) maximum curvature attributes, and (c) dip magnitude attribute. (d) Structural relief map along the Hulett marker. The surface structure map was calculated assuming average formation velocity of 14,000 ft/s, with the contours drawn every 25 feet. Black lines indicate fault traces interpreted along the Hulett horizon. The circular curves indicate salt collapse faults. The star symbol indicates the PRB #1 well projection.

Extreme curvature analysis.

Extracting detailed information about fractures is fundamental to successful carbon storage. This is particularly the case with low-permeability, tight sand reservoirs like the Hulett Member of the Sundance Formation, or the Minnelusa Formation. Unfortunately, obtaining detailed fracture information at the DFS storage site is difficult because of the lack of direct observational data in the subsurface. Therefore, it is important to apply new algorithms that help to resolve structural details that are otherwise not easily discernible from conventional seismic attributes.

Among various geometric attributes, we found extreme curvature and its associated azimuth to be the most valuable attributes for fracture mapping. In a 3D space, curvature is nonunique because it depends on evaluation direction (Roberts, 2001). The extreme curvature algorithm searches for the highest possible intensity and the most likely azimuthal direction in which there is the highest potential for fractures to develop (Gao and Di, 2015). Curvature reaches its absolute maximum at a specific azimuth where curve shape is the tightest, which is defined as extreme curvature and the corresponding azimuth being extreme curvature azimuth. An advantage of extreme curvature over other curvature types is that it delineates domains with enhanced potential to develop fractures (Gao and Di, 2015).

Figure 14 shows extreme curvature and extreme curvature azimuth extracted along the Hulett and Minnelusa stratigraphic intervals. Compared to other geometric attributes (Figures 10 and 13), extreme curvature and azimuth reveal more structural details of the fractured reservoirs. Specifically, extreme curvature azimuth shows that the northwest-trending lineaments dominate along the Hulett horizon and overprint northeast-trending features, which are more readily visible at the lower stratigraphic Minnelusa horizon (Figure 14).

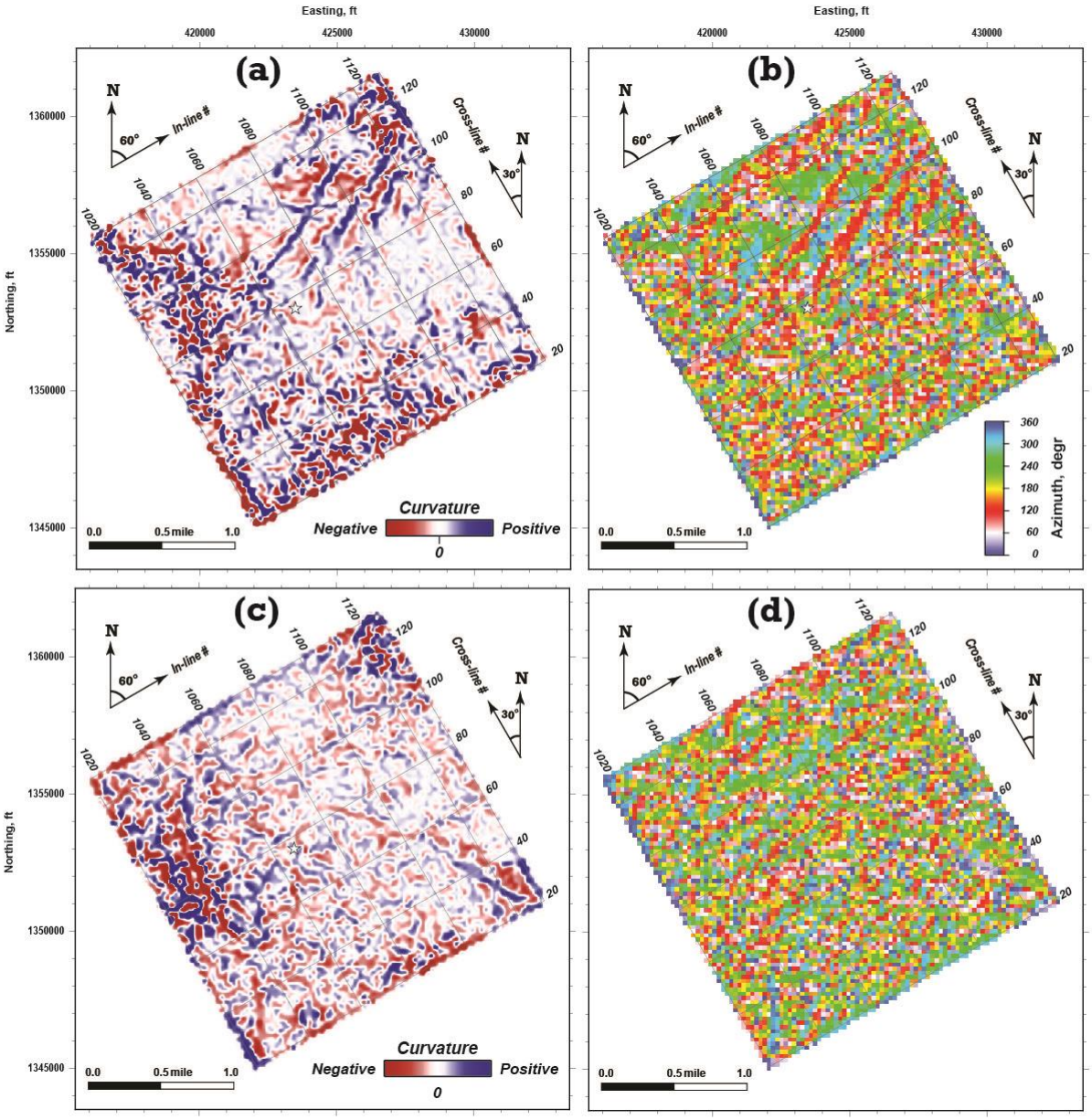

Figure 14. Geometric attributes extracted along the major reservoir horizons at DFS storage site. (a) Extreme curvature and (b) extreme curvature azimuth along the Hulett marker, and (c) extreme curvature and (d) extreme curvature azimuth along the Minnelusa marker.

Azimuthal velocity analysis.

Velocity Variations with Azimuth (VVAz) analysis has been performed as described above using in-house software. Fast and slow normal-moveout velocity, V_{nmo}, and their directions were calculated for every data sample of the DFS seismic volume. Figure 15 shows the percentage of anisotropy (fracture intensity) and direction of the fast P-wave velocity extracted from the corresponding volumes along the Hulett marker. Taken together these properties allow addition of meso-scale fracture permeability to geologic models.

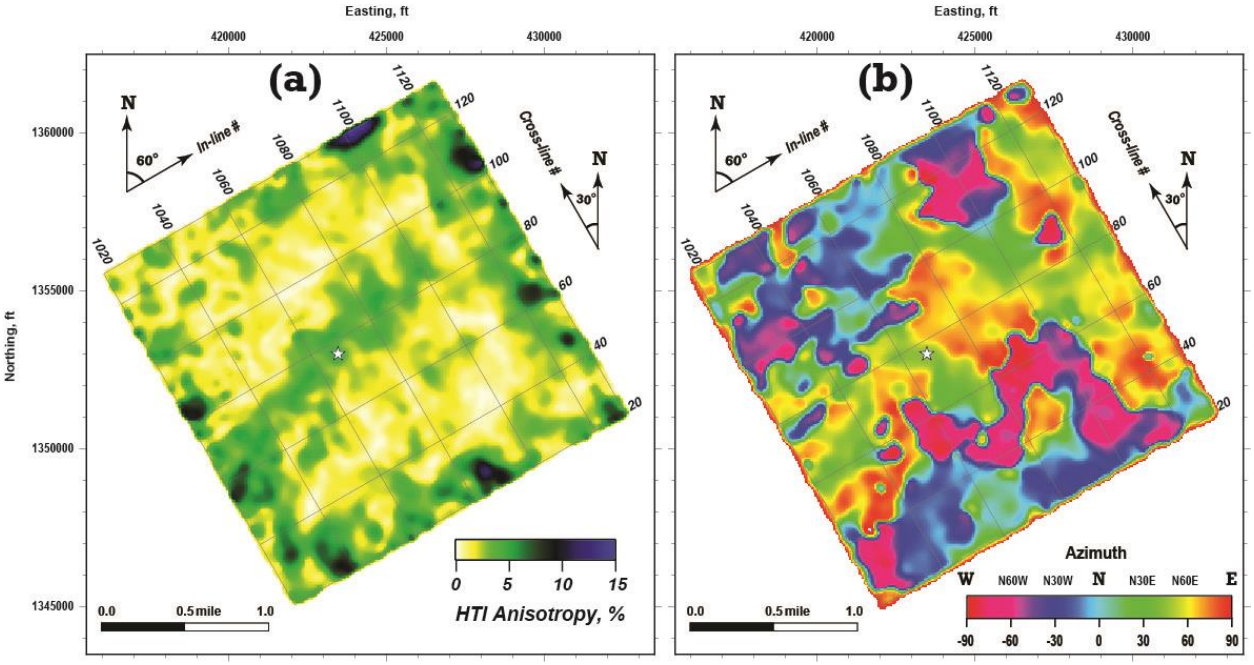

Figure 15. (a) Map of the fracture intensity (with dark colors indicating increased fracture density) and (b) map of the fast P-wave velocity azimuth (parallel to fractures direction) along the Hulett marker. The star symbol indicates the PRB#1 well projection.

There is a broad zone of intense (~5% anisotropy) fracturing trending northeast, which crosses the PRB#1 well location (Figure 15a). The same northeast azimuthal direction characterizes the fast seismic-wave propagation (Figure 15b) in the PRB#1 vicinity. Note that this is the preferred direction, along which fractures may enhance injection/production rates for the well. A total of 12,321 measurements of fast velocity direction along the Hulett marker were used to build azimuthal distribution histogram and the corresponding bidirectional rose diagram (Figure 16). The azimuthal distribution plots clearly demonstrate two major trends in fast velocity orientation, the northeast and northwest. These two general directions fit well with the analysis of Landsat

images (Marrs and Raines, 1984) and the congregation of published lineament and lineament zones for the Powder River Basin provided by Anna (2009).

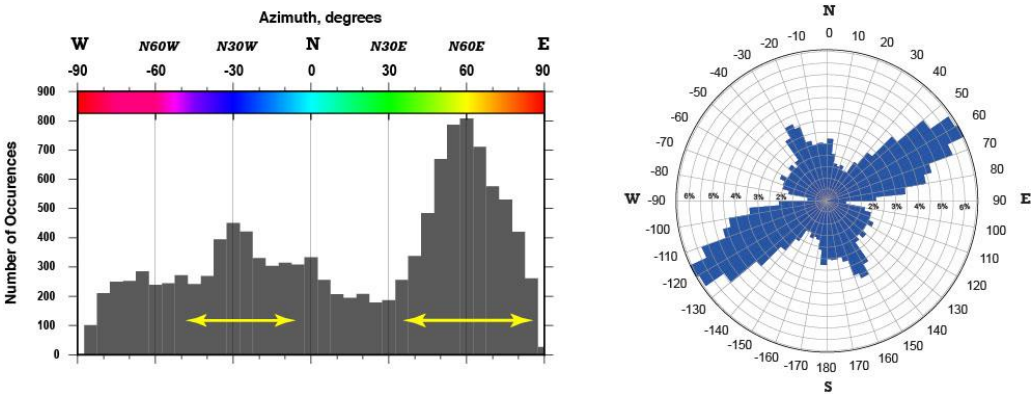

Figure 16. Azimuthal distribution histogram (left panel) and the corresponding rose diagram (right panel) showing bidirectional (symmetric) azimuthal distribution of the fast velocity measurements along the Hulett marker of the DFS study site. Yellow arrows, drawn over the histogram, designate azimuthal range of surface lineaments mapped from the Landsat images.

The amount of information provided by the VVAz volumes is huge and understanding its merit is still an ongoing process. We have prepared the fracture intensity and fracture direction maps for all targeted formations including the reservoir and seal rocks, but the Minnelusa marker will conclude the azimuthal anisotropy discussion in this paper. Figure 17a shows localities with elevated anisotropy (dark colors) along the Minnelusa marker. As in case with the Hulett horizon, we interpret them to be associated with zone of intense fracture development, and hence high preferential permeability. In the PRB#1 vicinity, these fractures are oriented in the northeast direction (Figure 17b). Figure 18 highlights the overall azimuthal fracture distribution along the Minnelusa for the DFS site. And again, the northeast and northwest are two major directions defining the previously observed fracture orientation trends. These two directions are also consistent with lineament orientations determined by discontinuity analysis of post-stack seismic attribute volumes.

The seismic data analysis presented in this paper, including discontinuity and VVAz, demonstrate potential of faults and fracture development in the DFS storage complex. Different fault-generation mechanisms were revealed in this study, namely basement-involved faulting and rock salt dissolution.

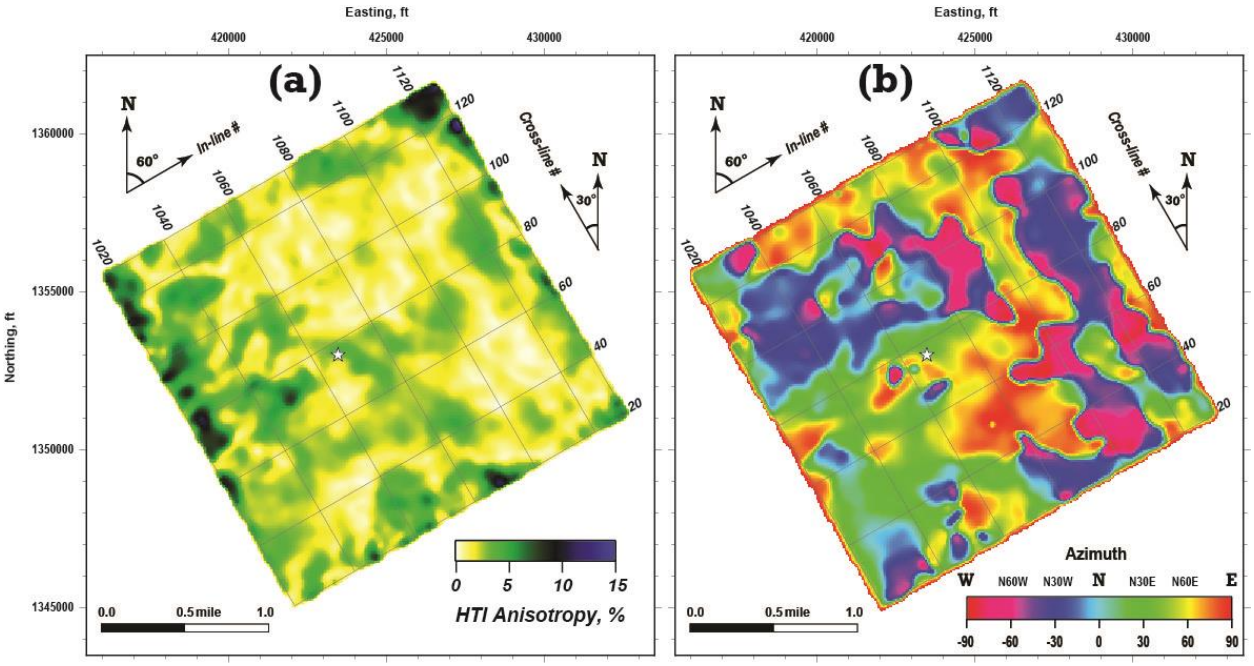

Figure 17. (a) Map of the fracture intensity (with dark colors indicating increased fracture density) and (b) map of the fast P-wave velocity azimuth (parallel to a fractures strike direction) along the Minnelusa marker. The star symbol indicates the PRB#1 well projection

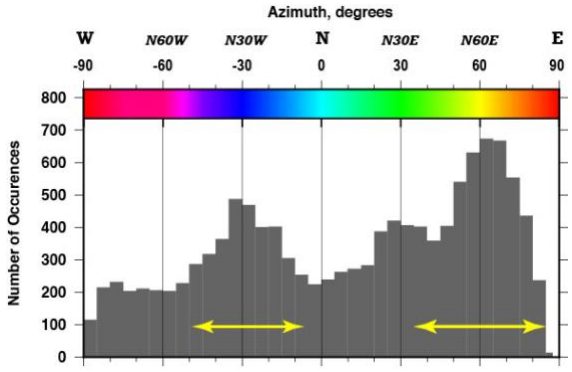

Figure 18. Azimuthal distribution histogram of the fast velocity measurements along the Minnelusa marker of the DFS study site. Yellow arrows, drawn over the histogram, designate azimuthal range of surface lineaments mapped from the Landsat images.

Discussion and Conclusion

Faults are of major importance as potential fluid pathways for both the vertical and lateral migration of fluids in the subsurface (Bense et al., 2013). Assessing whether a fault forms a lateral flow barrier or a conduit for CO_2 is crucial to assessing the efficiency and safety of subsurface carbon storage, as faults are ubiquitous in sedimentary basins, and will naturally occur close to or within storage complexes. The scale and distribution of faults may vary depending on the type of sedimentary basin and its geological history. In particular, faults that are below the resolution of seismic surveys cannot be found and avoided (Lohr et al., 2008; Le Gallo, 2016). In fact, faults occur at many of the first commercial- and pilot-scale CO_2 storage sites located in sedimentary basins (e.g., In Salah, Algeria, Mathieson et al., 2010; Snøvhit, Norway, Chiaramonte et al., 2011; Ketzin, Germany, Martens et al., 2012; Otway, Australia, Hortle et al., 2013). Therefore, the study of the behavior of faults to act as a barrier or fluid conduit becomes an essential element for the success of any long-term CO_2 storage project such as at DFS storage site. It has been observed in some hydrocarbon reservoirs that faults that were initially acting as barriers started acting as conduits when the pressure differential across the fault was increased due to hydrocarbon production (Yielding, et al., 1997). Therefore, fault-related fluid flow can vary with time, and thus represents a four-dimensional process. Johri et al. (2014) characterized the faults as a sandwich of permeable fractured rock damage zones on either side of a relatively impermeable fault core. Due to this complexity, extreme heterogeneities may exist in the fault damage zones over very small spatial distances. Therefore, the study of fluid migration across the fault, laterally along the fault, and vertically up and down the fault is an important element of the risk assessment process for potential CO_2 storage formations with existing faults.

Faults introduce a challenge not only in the character of fluid migration in the subsurface. Fluid injection has also the potential to induce earthquakes, from microseismicity to magnitude 5+ events (White and Foxall, 2016). As the injected fluid displaces the in-situ brine, a large overpressure plume develops with the extent of pressure perturbation that is typically much larger than the CO_2-rich plume. If the storage reservoir is intersected by moderately large, pre-

existing fault, the pressure plume can interact with the fault, and potentially trigger fault slip (White and Foxall, 2016). It is commonly observed that many faults stay in a state of critical equilibrium under in-situ stresses and formation fluid pressures. It is these critically stressed faults that pose the greatest challenge for subsurface fluid injection, since very small perturbations in stress or pore pressure can induce slip (Zoback and Gorelick, 2012). The fault size appears to be one of the key factors controlling the maximum magnitude of seismic event. Figure 19 illustrates this relationship that White and Foxall (2016) have compiled from different researchers based by field observations.

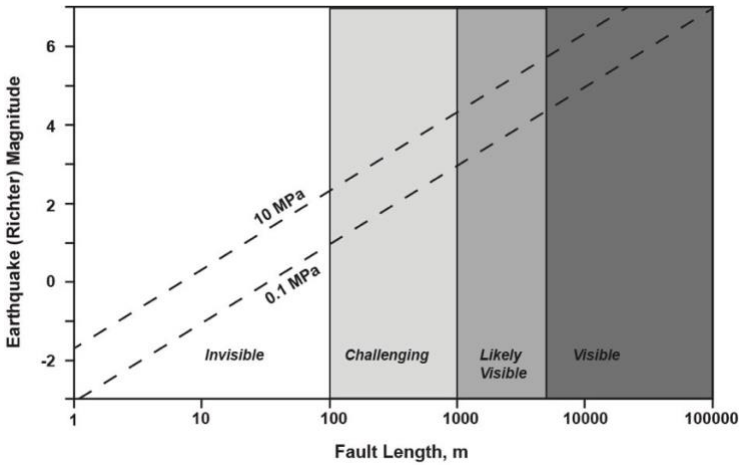

Figure 19. Scaling relationship between fault size and earthquake magnitude. Dashed lines indicate a commonly observed range of stress drop, from 0.1 to 10 MPa. Vertical shaded regions indicate "typical" visibility of a given size fault using 3D seismic. Modified from White and Foxall (2016).

Thus, relatively small-size faults, extending for only several hundred meters along a repository formation, may potentially cause some damage at the surface if the earthquake magnitude reaches 4 or 5. As for DFS study site, there are several fault traces along the targeted horizons (Figures 10 through 13) that are long enough that the method of White and Foxall (2016) suggest they could cause seismic events of 5+ magnitude. Our primary concern is related to the northwest-trending fault located just north of PRB#1 well. While it is often difficult to detect individual faults and their main parameters, fault populations tend to follow well-established statistical distributions in terms of their direction and density. It is sometimes possible to constrain these distributions using seismic azimuthal data as it was done in this study. The inferred fracture orientation and fracture density can then be used to examine the probability of similar faults encountering the propagating pressure front and/or CO_2 front. Moreover,

knowledge of fracture densities and locations in a tight sand reservoir may serve as a predictor of injection/production rates. To avoid hazardous situations, the faults and fracture zones mapped in this study should be addressed before the full-scale CO_2 injection begins. The potential for reactivation can be assessed using in-situ stress estimates and hydromechanical simulations (Chiaramonte et al., 2014).

Although triggering earthquakes during fluid injection may be potentially hazardous, our principal concern in this study is the seal integrity of the CO_2 repositories. Given large volumes of CO_2 (50+ million metric tons) to be injected into selected formations for over a 30-year timeframe in the vicinity of DFS, even a small-size earthquake triggered by the injection could jeopardize the seal integrity of the storage formation. Fault reactivation may induce seal rupture with the possibility of connecting the reservoir with other rock blocks and the surface. The laboratory studies show that just a few millimeters of shear displacement are capable of enhancing fracture permeability and several centimeters of slip would be capable of creating a permeable hydraulic pathway that could compromise the seal integrity of the CO_2 reservoir, and potentially propagate to the surface (Zoback and Gorelick, 2012). Therefore, in light of the risk posed by even small- to moderate-sized earthquakes, formations suitable for large-scale injection of CO_2 must be carefully chosen. Besides to being well sealed by impermeable overlaying strata, they should be very porous, permeable and laterally extensive to accommodate large volumes of CO2 with minimal pressure increases. In the view of preexisting crustal faults revealed in this study, pressure buildup in the storage reservoirs is expected to be a primary source of risk associated with CO_2 storage. In order to minimize this risk, storage reservoir pressure will need to be carefully managed at least until injection ceases, and likely monitored for a significant amount of time after that.

The costs of active pressure management include expenses for extracting in-situ formation fluids, processing them, and then disposing of them. This contrasts with far lower costs of passive pressure management, where the pressure is allowed to normalize through natural migration of fluids out of the reservoir. If active pressure management is required but the costs of this risk mitigation technology are prohibitive, then a part or the whole storage reservoir may not meet economic feasibility criteria for CO2 storage capacity under current regulations (Pawar et al., 2015; Anderson, 2017).

Numerous salt dissolution sinkholes, revealed with the DFS-3D seismic, introduce more geologic complexity and associated uncertainty in flow predictions. These faults vary in size, but they all have elliptical closed shapes and originate at the Ervay Salt horizon (Figure 20).

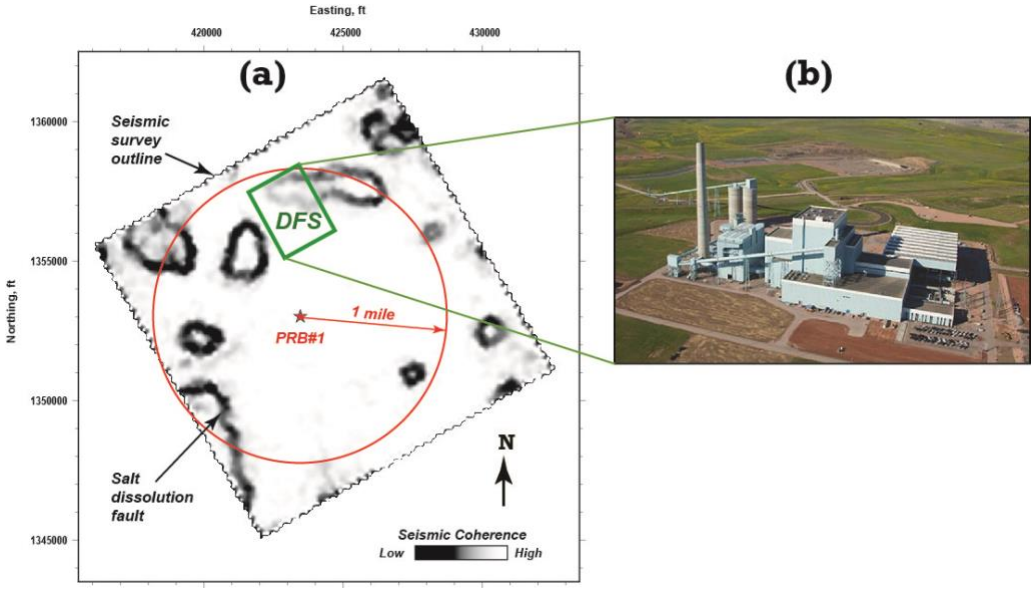

Figure 20. Salt dissolution faults (a) mapped using seismic coherence attribute extracted along the Ervay Salt marker. Note the Dry Fork Station (DFS) facilities (b) located over one of the structural depressions and five more salt dissolution faults located within a one-mile radius around the PRB#1 injection well.

Injection into formations either above or below the Ervay Salt could expedite its dissolution. If faults or other flow paths allow fluids to migrate from the shallower Hulett and Lakota, downward along the highly permeable fault damage zones (Johri et al., 2014), and pressure and buoyancy effects to not stop this migration before it reaches the rock salt layer, then it will intensify the natural dissolution. Injection into the underlying Minnelusa sands poses a greater risk to the Ervay Salt as buoyancy and pressure effects would be less likely to slow or stop fluid migration upward along basement-involved faults (Figure 10d). Both of the described scenarios may lead to environmental and safety hazards that must be addressed through the hydromechanical modeling (Zhang et ai., 2007; Wei et al., 2016; Zulqarnain et al., 2020). Fault seal modelling is associated with significant uncertainties arising from the limited subsurface data, resolution of seismic data, faulting mechanics, fault zone structure, spatial and temporal variations, and overall limitations of the scalability of observations. Nonetheless, several models to estimate the sealing properties of faults have been developed and successfully used to predict hydrocarbon column heights. However, for the fault seal modelling of CO_2 reservoirs the

wettability of the CO_2–brine–rock system introduces additional uncertainties. If faults pose a risk to this project, the injection pressures, and total volume of CO_2 stored may have to be reduced.

There are a number of potential issues to consider before using deep saline aquifers such as the Minnelusa or Hulett for CO_2 storage, the most important of which are the safety of these potentially large-scale reservoirs and uncertainty associated with the spatial distributions of petrophysical and mechanical parameters which guide geological modeling. Indeed, there is not much historical exploration of deep saline formations in the DFS area, and a lack of permeability data can be a significant source of uncertainty about the risks of storage in these formations. The reasons for using saline aquifers for CO_2 storage is that they are volumetrically large, widely distributed, and available near most sources of CO_2. Acknowledging the risks posed by salt dissolution and fluid migration along faults will allow judicious application of modeling and further investigation. By both understanding these risks better, and devising solutions an ultimately safer project is possible. For such large-scale injection as is planned at DFS, the geomechanics will play a key role in site-specific risk analysis. Therefore, to ensure safe operations, we would recommend a practical learning approach, involving a gradual increase of injection rates combined with continuous monitoring of geomechanical changes within the reservoirs.

References

Aarre, V., D. Astratti, T. Al Dayyani, S. Mahmoud, A. Clark, M. Stellas, J. Stringer, B. Toelle, O. Vejbaek, and G. White, 2012, Seismic Detection of Subtle Faults and Fractures: Oilfield Review, **24**, no. 2, 28-43.

Alkhalifah, T., and I. Tsvankin, 1995, Velocity analysis for transversely isotropic media, Geophysics, **60**, p. 1550–1566.

Alkhalifah, T., 1997, Seismic data processing in vertically inhomogeneous TI media, Geophysics, **62**, p. 662–675.

Anderson, S.T., 2017, Risk, Liability, and Economic Issues with Long-Term CO2 Storage – A Review, Natural Resources Research, **26(1)**, p. 89-112.

Anna, L.O., 2009, Geologic assessment of undiscovered oil and gas in the Powder River Basin: U.S. Geological Survey Digital Data Series DDS-69-U, 93 p.

Bense, V. F., Gleeson, T., Loveless, S. E., Bour, O., and J. Scibek, 2013, Fault zone hydrogeology, Earth-Sci. Rev., **127**, p. 171–192.

Blumentritt, C., K. Marfurt, and E. Sullivan, 2006, Volume-based curvature computations illuminate fracture orientations — Early to mid-Paleozoic, Central Basin Platform, west Texas: GEOPHYSICS, **71**, no.5, p. B159–B166.

Calvert, A., E. Jenner, R. Jefferson, R. Bloor, N. Adams, R. Ramkhelawan, and C. St. Clair, 2008, Wide azimuth imaging and azimuthal velocity analysis using offset vector tile prestack migration: First Break, **26**, p. 103-107.

Chiaramonte, L., Johnson, S., and J.A. White, 2011, Preliminary Geomechanical Analysis of CO_2 Injection at Snøhvit, Norway, in: ARMA-11-441, American Rock Mechanics Association, ARMA, San Francisco.

Chiaramonte, L., White, J.A., and W. Trainor-Guitton, 2014, Probabilistic geomechanical analysis of compartmentalization at the Snøhvit CO2 sequestration project, J. Geophys. Res.: Solid Earth **120(2)**, p. 1195-1209.

Chopra, S., 2001, Coherence Cube- a promising tool: GEOHORIZONS, p. 11-15.

Chopra, S. and K. Marfurt, 2007, Volumetric curvature attributes add value to 3D seismic data interpretation", The Leading Edge, **26**, p. 856-867.

Chopra, S., S. Misra, and K. Marfurt, 2011, Coherence and curvature attributes on preconditioned seismic data, The Leading Edge, **30**, p. 386-393.

Chopra, S., V. Sudhakar, G. Larsen, and H. Leong, 2000, Azimuth-based coherence for detecting faults and fractures, World Oil Magazine, September 2000, p. 5-62.

Dix, C.H., 1955, Seismic velocities from surface measuremnts: Geophysics, **20**, p. 68-86.

Dulaijan, K. and G. Margrave, 2015, Azimuthal velocity analysis of 3D seismic for fractures: Altoment-Bluebell field, CREWES Research Report, 27, p. 1-15.

Endres, H., R. Samiee, C. Krawczyk, D. Tanner, H. Trappe, O. Oncken, and P. Kukla, 2005, Sub-seismic deformation processes in clastic reservoirs derived from dip and azimuth steered coherency processing, SEG Technical Program, Expanded Abstracts, p. 1382-1385.

Fomel, S., 2004, On anelliptic approximation for qP velocities in VTI media: Geophys. Prosp., **52**, p. 247-259.

Gao, D., and H. Di, 2015, Extreme curvature and extreme flexure analysis for fracture characterization from 3D seismic data: New analytical algorithms and geologic implications, Geophysics, **80**, NO.2, p. IM11-IM20

Grechka, V., and I. Tsvankin, 1998, 3-D description of normal-moveout in anisoropic inhomogeneous media, Geophysics, **63**, p. 1079-1092

Hortle, A., Xu, J., and T. Dance, 2013, Integrating hydrodynamic analysis of flow systems and induced-pressure decline at the Otway CO_2 storage site to improve reservoir history matching, Mar. Pet. Geol., **45**, p. 159–170.

Jenner, E., M. Williams, and T. Davis, 2001, A new method for azimuthal velocity analysis and application to a 3D survey, Weyburn field, Saskatchewan, Canada: SEG Technical Program, Expanded Abstracts, p. 102-105.

Johri, M., M. Zoback, and P. Hennings, 2014, A scaling law to characterize fault-damage zones at reservoir depth, AAPG Bulletin, **98(10)**, p. 2057-2079.

Kazmi, H., A. Alam, S. Ahmad, and A. Shafiq, 2012, Fault characterization using volumetric curvature from continuous phase spectrum: SEG Technical Program, Expanded Abstracts, p. 2012-0445.

Keranen, K. M., M. Weingarten, G. A. Abers, B. A. Bekins, and S. Ge, 2014, Sharp increase in central Oklahoma seismicity since 2008 induced by massive wastewater injection. *Science* **345(6195)**, p. 448-451.

Le Gallo, Y., 2016, Hydro-mechanical influence of sub-seismic blind faults on integrity of CO_2 geological storage in deep saline aquifer, Int. J. Greenh. Gas Con., 51, p. 148–164.

Lichtner, D.T, R. Toner, J. Wrage, and R. Lynds, 2020, Upper Cretaceous Strata in the Powder River Basin: Formation Tops Database, Structure and Thickness Contour Maps, and Associated Well Data, Wyoming State Geological Survey Open File Report **2020-9**.

Lohr, T., C. Krawczyk, D. Tanner, R. Samiee, H. Endres, P. Thierer, O. Oncken, H. Trappe, R. Bachmann, and P. Kukla, 2008, Prediction of subseismic faults and fractures: Integration of three-dimensional seismic data, three-dimensional retrodeformation, and well data on an example of deformation around an inverted fault: AAPG Bulletin, **92**, no. 4, p. 473–485

McLaughlin, F., S. Quillinan, K. Coddington, Yu. Ganshin, E. Phillips, Z. Jiao, H. Wang, M. Johnson, D. Bagdonas, C. Nye, N. Bosshart, and B. Oster, 2021, Wyoming CarbonSAFE: advancing commercialization of low-carbon energy technologies in fossil-rich Wyoming, 15th International Conference on Greenhouse Gas Control Technologies, GHGT-15, 15th – 18th March 2021, Abu Dhabi, UAE

Mai, H., K. Marfurt, and S. Chávez-Pérez, 2009, Coherence and volumetric curvatures and their spatial relationship to faults and folds, an example from Chicontepec Basin, Mexico: SEG Technical Program, Expanded Abstracts, p. 1063-1067.

Marfurt, K.J, 2006, Robust estimates of 3D reflector dip and azimuth, Geophysics, **71(4)**, p. 29-40.

Marrett, R., and R. Allmendinger, 1991, Estimates of strain due to brittle faulting: Sampling of fault populations, Journal of Structural Geology, **13**, p. 735–738.

Marrs, R. and G. Raines, 1984, Tectonic Framework of the Powder River Basin, Wyoming and Montana, Interpreted from Landsat Imagery, The American Association of Petroleum Geologists, **68(11)**, p. 1718-1731.

Martens, S., Kempka, T., Liebscher, A., Lüth, S., Möller, F., Myrt- tinen, A., Norden, B., Schmidt-Hattenberger, C., Zimmer, M., Kühn, M., and T.K. Group, 2012, Europe's longest-operating onshore CO_2 storage site at Ketzin, Germany: a progress report after three years of injection, Environ. Earth Sci., **67**, p. 323–334.

Mathieson, A., Midgley, J., Dodds, K., Wright, I., Ringrose, P., and N. Saoul, 2010, CO_2 sequestration monitoring and verification technologies applied at Krechba, Algeria, The Leading Edge, **29**, p. 216–222.

Michelena, R., K. Godbey, H. Wang, J. Gilman, and C. Zahm, 2013, Estimation of Dispersion in Orientations of Natural Fractures from Seismic Data: Application to Discrete Fracture Network Modeling: Society of Petroleum Engineers, SPE 168791.

Nelson, R., 2001, Geologic analysis of naturally fractured reservoirs: Elsevier.

Pawar, R, J., Bromhal, G. S., Carey, J. W., Foxall, W., Korre, A., Ringrose, P. S., Tucker, O., Watson, M. N., White, J. A., 2015, Recent advances in risk assessment and risk management of geologic CO_2 storage. Int. J. Greenh. Gas Control, **40**, p. 292-311.

Roberts, A., 2001, Curvature attributes and their application to 3D interpreted horizons, First Break, **19(2)**, p. 85-100.

Thomas, G.E., 1971, Continental plate tectonics, southwest Wyoming, *in* Symposium on Wyoming tectonics and their economic significance: Wyoming Geological Survey, 23rd Annual Field Conference Guidebook, p. 103-123.

Walsh, J., J. Watterson, A. Heath, P. Gillespie, and C. Childs, 1998, Assessment of the effects of sub-seismic faults on bulk permeabilities of reservoir properties: Geological Society London Special Publications, **127**, no. 1, p. 99-114.

Walsh, F. R., and M. D. Zoback. 2015, Oklahoma's recent earthquakes and saltwater disposal. *Science Advances* 1(5).

Wei, X., Q. Li, X. Li, and Z. Niu, 2016, Modeling the hydromechanical responses of sandwich structure faults during underground fluid injection, Environ. Earth Sci., **75,** Article number: 1155

White, J.A., and W. Foxall, 2016, Assessing seismicity risk at CO_2 storage projects: Recent progress and remaining challenges, International Journal of Greenhouse Gas Control, **49**, p. 413-424.

Williams, M. and E. Jenner, 2002, Interpreting seismic data in the presence of azimuthal anisotropy; or azimuthal anisotropy in the presence of the seismic interpretation, The Leading Edge, **21**, p. 771-774.

Yielding, G., Freeman, B., and D.T. Needham, 1997, Quantitative fault seal prediction, AAPG Bulletin, **81(6)**, p. 897–917.

Zhang, X., Koutsabeloulis, N., and K. Heffer, 2007, Hydromechanical modeling of critically stressed and faulted reservoirs, AAPG Bulletin, **91**(**1**), p. 31–50

Zoback, M. D., and S. M. Gorelick, 2012, Earthquake triggering and large-scale geologic storage of carbon dioxide: Proc. Natl. Acad. Sci. USA, **109(26)**, p. 10164-10168.

Zulqarnain, M., Zeidouni, M., and R.G. Hughes, 2020, Hydromechanical modeling to evaluate impact of fault structure on CO_2 migration in stacked storage system, International Journal of Greenhouse Gas Control, **93**, 102886